

## Substorm-Ring Current Coupling: A Comparison of Isolated and Compound Substorms

## Key Points:

- Quantitative estimates of ring current energy for compound and isolated substorms are shown
- The energy content and postonset enhancement is larger for compound compared to isolated substorms
- Solar wind coupling is a key driver for differences in the ring current between isolated and compound substorms

## Supporting Information:

- Supporting Information S1
- Figure S1
- Figure S2
- Figure S3
- Figure S4

## Correspondence to:

J. K. Sandhu,  
j.sandhu@ucl.ac.uk









## Citation:

Sandhu, J. K., Rae, I. J., Freeman, M. P., Gkioulidou, M., Forsyth, C., Reeves, G. D., et al. (2019). Substorm-ring current coupling: A comparison of isolated and compound substorms. *Journal of Geophysical Research: Space Physics*, 124. <https://doi.org/10.1029/2019JA026766>

Received 27 MAR 2019

Accepted 30 JUL 2019

Accepted article online 7 AUG 2019

J. K. Sandhu<sup>1</sup> , I. J. Rae<sup>1</sup> , M. P. Freeman<sup>2</sup> , M. Gkioulidou<sup>3</sup> , C. Forsyth<sup>1</sup> , G. D. Reeves<sup>4</sup> , K. R. Murphy<sup>5</sup> , and M.-T. Walach<sup>6</sup> 

<sup>1</sup>Department of Space and Climate Physics, Mullard Space Science Laboratory, University College London, London, UK, <sup>2</sup>British Antarctic Survey, Cambridge, UK, <sup>3</sup>Applied Physics Laboratory, John Hopkins University, Baltimore, MD, USA, <sup>4</sup>Los Alamos National Laboratory, Los Alamos, NM, USA, <sup>5</sup>Department of Astronomy, University of Maryland, College Park, MD, USA, <sup>6</sup>Physics Department, Lancaster University, Lancaster, UK

**Abstract** Substorms are a highly variable process, which can occur as an isolated event or as part of a sequence of multiple substorms (compound substorms). In this study we identify how the low-energy population of the ring current and subsequent energization varies for isolated substorms compared to the first substorm of a compound event. Using observations of H<sup>+</sup> and O<sup>+</sup> ions (1 eV to 50 keV) from the Helium Oxygen Proton Electron instrument onboard Van Allen Probe A, we determine the energy content of the ring current in L-MLT space. We observe that the ring current energy content is significantly enhanced during compound substorms as compared to isolated substorms by ~20–30%. Furthermore, we observe a significantly larger magnitude of energization (by ~40–50%) following the onset of compound substorms relative to isolated substorms. Analysis suggests that the differences predominantly arise due to a sustained enhancement in dayside driving associated with compound substorms compared to isolated substorms. The strong solar wind driving prior to onset results in important differences in the time history of the magnetosphere, generating significantly different ring current conditions and responses to substorms. The observations reveal information about the substorm injected population and the transport of the plasma in the inner magnetosphere.

## 1. Introduction

Substorms are an impulsive phenomenon associated with the storage and release of energy in the Earth's magnetosphere. Based on auroral observations, it was proposed that substorms can be described as the occurrence of three separate phases: the growth phase, the expansion phase, and the recovery phase (Akasofu, 1968; McPherron, 1970). Overall, a substorm typically lasts 2–4 hr (Tanskanen, 2009). During the growth phase, low-latitude dayside reconnection with the IMF (interplanetary magnetic field) dominates over the nightside reconnection rate, resulting in an accumulation of open field lines in a highly stretched magnetotail (Kokubun & McPherron, 1981; McPherron, 1970, 1972; Milan et al., 2007). Substorm onset marks the beginning of the substorm expansion phase, and during the onset process rapid bursts of nightside reconnection close significant amounts of flux in the magnetotail (e.g., Hones & Schindler, 1979; Hubert et al., 2006). The dipolarization of the magnetic field and the destabilization of the near-Earth tail act to energize particles and drive intense electric currents (e.g., Forsyth et al., 2014; McPherron et al., 1973). The magnetosphere then enters the substorm recovery phase, where the nightside reconnection rate gradually subsides and the system returns to its original state. The occurrence of a substorm has wide ranging and substantial implications for the global magnetosphere and ionosphere. In this study we focus on the impact of substorms on the inner magnetosphere, specifically on the ring current population.

The terrestrial ring current is generated predominantly by ions with energies ranging from tens to hundreds of kiloelectron volts and resides mainly between 4 to 7 Earth Radii ( $R_E$ ; Daglis et al., 1999; Le et al., 2004; Sandhu et al., 2018). Substorm dipolarization following substorm onset is associated with the injection of plasma to the inner magnetosphere, typically affecting ring current ions with hundreds of electron volts (eV) to tens of kiloelectron volt (keV) energies (Yue et al., 2018). However, previous work has shown that the injection of plasma into the inner magnetosphere is highly variable. It has been identified that only approximately 30% of substorms are associated with an observed classical injection signature in the inner magnetosphere (Boakes et al., 2011; Takada et al., 2006). Despite the variability of the injections, a study conducted by

Sandhu et al. (2018) demonstrated that, on average, the ring current experiences statistically significant enhancements following substorm onset. It was established that the global energy content, estimated from an energy range up to hundreds of kiloelectron volts covering the bulk population, increased by 12% relative to the preonset value, with the enhancement predominantly occurring within the substorm expansion phase. Sandhu et al. (2018) showed that the low-energy population of H<sup>+</sup> and O<sup>+</sup> ions with energies ranging up to 50 keV exhibited significant enhancements following substorm onset, with the energy content of these ions increasing by more than 50%. The energy range is consistent with the expected energy range of substorm-associated plasma injections in the inner magnetosphere (Yue et al., 2018), as well as the ion plasma sheet population convected earthward.

In this paper, we extend the analysis of Sandhu et al. (2018) to explore whether some substorm characteristics are more favorable to ring current energization than others. Specifically, we categorize substorms according to the level of additional substorm activity prior to and following an event. We define isolated substorms as those where there is no substorm activity prior to the event and after the event. Compound substorms are defined as occurring as part of a sequence of substorms where the recovery phase leads directly to the expansion phase of a succeeding substorm. Previous work has demonstrated differences in the solar wind driving and auroral evolution during compound substorms in comparison to isolated substorms (e.g., Kim et al., 2008; Liou et al., 2013; Newell & Gjerloev, 2011), such that compound substorms are typically associated with periods of high solar wind-magnetosphere coupling. However, the quantitative aspect of how a sequence of compound substorms as opposed to an isolated substorm can affect the inner magnetosphere, specifically the ring current population, remains poorly understood. In this study, we examine whether both types of substorms enhance the ring current population, focusing on the evolution and morphology of the low-energy ring current ion population.

## 2. Data and Method

The Van Allen Probes mission consists of two identically instrumented spacecraft: probe A and probe B (Mauk et al., 2013). The elliptical orbits have an inclination of 10°, a perigee of ~600-km altitude, and an apogee of 6 R<sub>E</sub> geocentric radial distance. The orbital period is 9 hr, and the precession of the orbital apogee allows sampling of all local times in less than 2 years. The coverage and low inclination of the Van Allen Probes orbit are highly suited to studying the ring current region. The probes are equipped with the Helium Oxygen Proton Electron (HOPE) mass spectrometers (Funsten et al., 2013; Spence et al., 2013). In this study we use the Level 3 HOPE observations of omnidirectional energy fluxes for H<sup>+</sup> and O<sup>+</sup> ions, with an energy range from 1 eV to 50 keV. For this statistical study we take all observations obtained during 2012 to 2018. We note that the energy range was selected to focus on the injected and convected ion population that is particularly sensitive to substorm onset (Sandhu et al., 2018; Yue et al., 2018), and the energy range is not representative of the full ring current population. It is known that higher energies also exhibit energization, as injections are observed to range up to several hundreds of kiloelectron volts (e.g., Sandhu et al., 2018; Turner et al., 2017).

The omnidirectional ion fluxes obtained from HOPE are used to estimate the energy content for both the H<sup>+</sup> and O<sup>+</sup> data sets. The same method as detailed by Sandhu et al. (2018; adapted from Gkioulidou et al., 2016) is applied to the data and will now be briefly summarized. The omnidirectional ion energy flux,  $j(E_{\text{ch}})$ , at the instrument energy channels,  $E_{\text{ch}}$ , is taken for a given data set. The partial energy density,  $\epsilon$ , is then calculated with a temporal resolution of 5 min using the following equation:

$$\epsilon = \sum_{E_{\text{ch}}} 2\pi \sqrt{2E_{\text{ch}} m} j(E_{\text{ch}}) \Delta E_{\text{ch}} \quad (1)$$

where  $\Delta E_{\text{ch}}$  is the energy channel bin width and  $m$  is the ion mass. For a given 5-min time bin, we then consider the volume,  $\delta V(L)$ , which is the volume of the dipole magnetic field intersecting the area defined by the range of  $L$  shells traversed in the time interval and 6 hr of magnetic local time (MLT). The full details of how this volume is determined are provided in the supporting information (Text S1). The partial energy density,  $\epsilon$ , is multiplied by the volume,  $\delta V(L)$ , to provide an estimate of the energy contained within the volume for each 5-min time bin,  $E_{5\text{min}}$ . The final step taken is to determine the total energy,  $E$ , contained within a spatial L-MLT bin. As a spacecraft traverses through the range of  $L$  values encompassed by a bin of

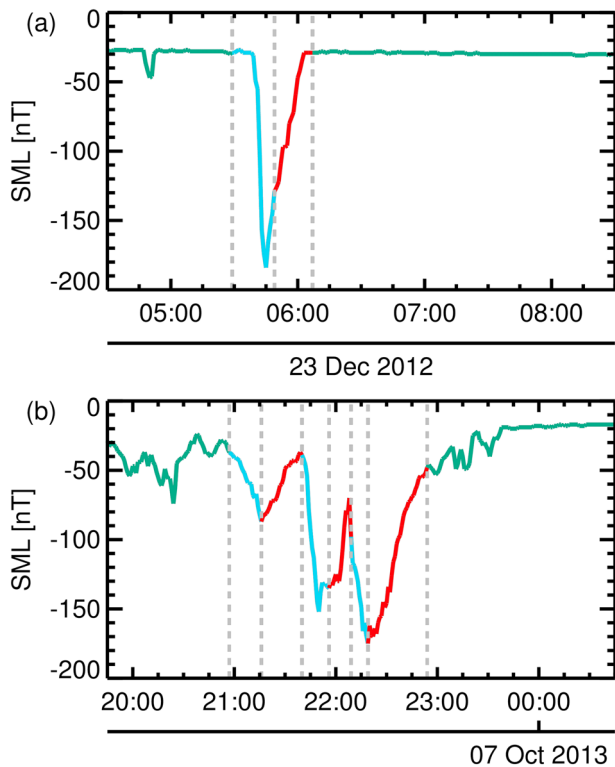


**Figure 1.** The SML index (nT) plotted as a function of time showing examples of (a) an isolated substorm and (b) a sequence of compound substorms. The color coding indicates the substorm phases as identified using the Substorm Onsets and Phases from Indices of the Electrojet technique. Green corresponds to the growth phase, blue corresponds to the expansion phase, and red corresponds to the recovery phase. The start times of the phases are also indicated by the vertical gray dashed lines.

width  $\Delta L$ , the energy values are summed. This is expressed by

$$E = \left[ \sum_{\Delta L} E_{5-\text{min}} \right] \left[ \frac{\Delta L}{\sum \delta L} \right] \quad (2)$$

where we use a  $L$  bin width of  $\Delta L = 1$ . It is noted that the scaling factor shown in equation (2) accounts for spacecraft trajectories where the distance traversed by the spacecraft differs from the  $L$  extent of the bin (e.g., a partial pass through the bin). This method is applied to both the  $\text{H}^+$  and  $\text{O}^+$  HOPE data sets, covering the time period from 2012 to 2018. We thus obtain estimates of the energy content of  $L$ -MLT bins ( $L$  bin width of 1 and MLT bin width of 6 hr) for each ion data set. The final data set provides good coverage over all MLT values and over an  $L$  range from 3 to 7. This will allow analysis of the bulk ring current region, as well as an examination of local time variations.

In order to examine how the energy content values vary during the substorm process, the values are binned according to substorm phase. The substorm phase for a given time is identified by applying the Substorm Onsets and Phases from Indices of the Electrojet (SOPHIE) technique (Forsyth et al., 2015) to the SuperMAG SML index (Gjerloev, 2012; Newell & Gjerloev, 2011), using an expansion percentile threshold of 75. We note here that the SML index can be considered as an equivalent to the AL index. In brief, the SOPHIE technique evaluates the rate of change of the SML index with 1-min temporal resolution. The technique identifies the expansion and recovery phases from temporal gradients in the SML index and labels all other times as growth phases. The SOPHIE technique is illustrated in Figure 1, where the SML time series is displayed for two substorm periods. The color coding of the time series indicates the identified substorm phases, where green is the growth phase, blue is the expansion phase, and red is the recovery phase. Using this approach, 9,994 unique substorms are identified for the time period considered.

A key characteristic of the ring current is the large enhancements in energy content during geomagnetic storms (Akasofu et al., 1963; Gonzalez et al., 1994). It has been demonstrated that quiet time and storm time substorms exhibit important and fundamental differences in the characteristics of injections and the effects on the ring current (e.g., Reeves & Henderson, 2001). In this study, we focus solely on nonstorm time measurements, to reduce variability in energy values and focus on differences between the isolated and compound substorms. Storm periods are identified using the approach detailed by Murphy et al. (2018), based on an initial storm list developed by Turner et al. (2015). For full details, the reader is referred to both Turner et al. (2015) and Murphy et al. (2018). The storm list is used to exclude any measurements of the energy content that occur during a geomagnetic storm, and the following analysis is representative of nonstorm conditions only. The exclusion of storm times reduces the number of substorms in the analysis to 5,756.

For this analysis, it is also required that we differentiate between isolated substorms and compound substorms. Using the SOPHIE technique, the sequence of phases can be identified, as illustrated by the examples shown in Figure 1. Compound substorms are identified from sequences where there are multiple onsets of an expansion phase with no intermediate growth phases (see Figure 1b). Each of the onsets within a given sequence is classified as an individual compound substorm. In contrast, isolated substorms are periods flanked by growth phases where only one onset occurs (see Figure 1a). Overall, there are 2,116 isolated substorms and 1,349 compound substorm sequences (consisting of 3,640 individual compound substorms in total) identified.

### 3. Energy Content of Low-Energy Ring Current Ions

Using the estimated values of energy content, we assess how the energy contributed by ions with energies between 1 eV and 50 keV varies with respect to substorm onset for isolated and compound substorms. We

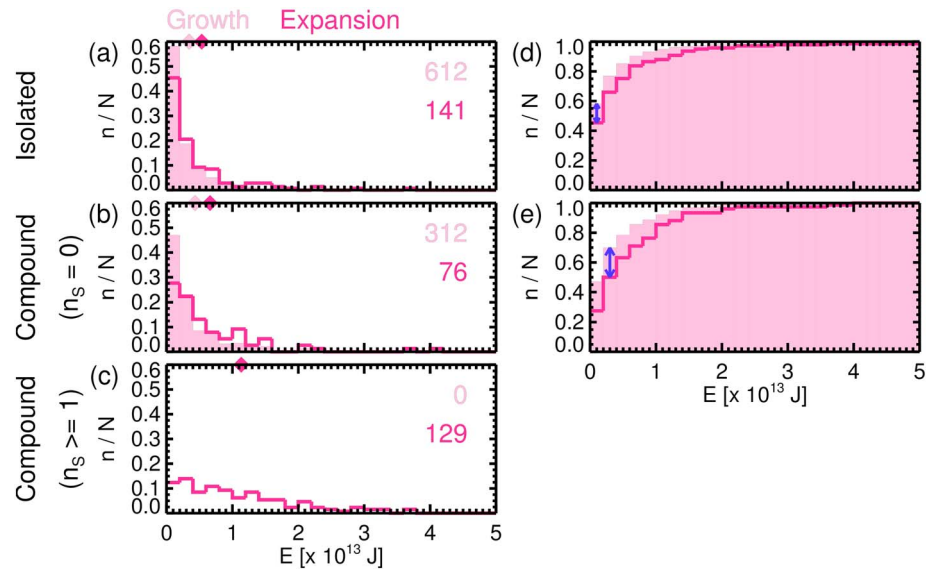


**Figure 2.** The (a–c) occurrence distributions and the (d, e) cumulative probability distributions of energy content values,  $E$  (J), for the spatial bin  $5 \leq L < 6$  and  $18 \leq MLT < 24$  for  $H^+$  ions. For each energy bin, the number of samples in the bin,  $n$ , is divided by the total number of samples in the distribution,  $N$ , to obtain the occurrence values. The pale-shaded distribution shows values during the growth phase, and the line distribution shows values during the expansion phase. The total number of samples in each distribution is labeled, and the mean value for each distribution is indicated by the diamonds, using the same color coding as the distributions. Each panel corresponds to a different category of substorms. We show (a, d) isolated substorms, (b, e) compound substorms for the first substorm in the sequence, and (c) compound substorms for the second or more substorms in the sequence. The cumulative probability distributions also indicate the Kolmogorov-Smirnov test statistic, shown by the blue arrow.

consider both  $H^+$  and  $O^+$  ions. In the following results we have chosen to focus on changes over onset, between the growth phase and expansion phase. Sandhu et al. (2018) demonstrated that the postonset enhancement of the ring current predominantly occurs during the expansion phase and that no significant further energization occurs during the substorm recovery phase.

Figures 2a–2c and 3a–3c show occurrence distributions of energy values,  $E$  (J), during the growth phase (shaded distribution) and the expansion phase (line distribution) for the spatial bin  $5 \leq L < 6$  and  $18 \leq MLT < 24$ . Cumulative probability distributions are also shown in Figures 2d, 2e, 3d, and 3e. Figure 2 corresponds to  $H^+$  ions, and Figure 3 corresponds to  $O^+$  ions. For each occurrence distribution, the mean value is indicated by the solid diamond at the top of the relevant panel and the number of points in the distribution is labeled, using the same color coding as the distribution. Furthermore, Figures 2 and 3 show occurrence distributions of energy content for isolated substorms (a, d) and compound substorms (b, c, e). The compound substorms are also further separated based on where they occur within the sequence. The number of preceding substorm expansion phases since the latest growth phase,  $n_s$ , is identified. Compound substorms that are the first of the sequence ( $n_s = 0$ ) correspond to panels (b) and (e). Substorm expansion phases that have followed the recovery phase of a preceding substorm ( $n_s \geq 1$ ) correspond to panel (c), and as the expansion phase was not preceded by a growth phase, there is no shaded distribution present. Although we focus on a single L-MLT bin in the premidnight sector for Figures 2 and 3, the same trends in the occurrence distributions are observed for the other spatial bins. The  $5 \leq L < 6$  and  $18 \leq MLT < 24$  bin was selected here because this region was observed to undergo the largest and most significant energization by Sandhu et al. (2018).

A comparison of Figures 2a–2c and 3a–3c indicates that the average energy values for the  $H^+$  ions typically range from  $0.4 \times 10^{13}$  J during the growth phases of isolated substorms (Figure 2a) up to  $1.3 \times 10^{13}$  J during the second and subsequent expansion phases of compound substorms (Figure 2c). The average energy values for the  $O^+$  ions range from  $0.2 \times 10^{13}$  J to  $0.5 \times 10^{13}$  J for the same cases (Figures 3a and 3c). Although the magnitudes of energy values are smaller for the  $O^+$  ions compared to the  $H^+$  ions, consistent trends are observed for both ion species, and we will focus on Figure 2 to describe these variations. Figures 2a and 2b show that the mean energy for the expansion phase is increased compared to the growth phase. Furthermore,

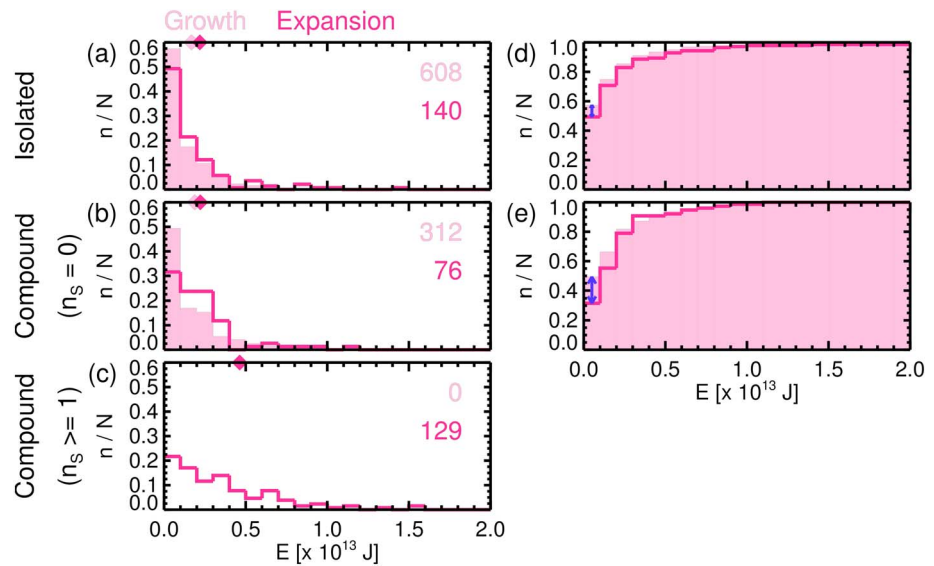


**Figure 3.** The occurrence distributions and cumulative probability distributions of energy content values for  $O^+$  ions, following the same format and color coding as Figure 2.

the difference in energy appears to be greater for compound substorms (Figure 2b) than for isolated substorms (Figure 2a). Figures 2a and 2b also show that the mean energy values are larger for compound substorms than isolated substorms, in both the growth and expansion phases. This indicates important differences in the energy content, as well as postonset changes in the energy content, between isolated and compound substorms. In terms of the compound substorms, Figure 2c shows that, for compound substorms following at least one previous onset in the sequence, the distribution is observed to be much broader compared to the distribution for the first substorm in a sequence (Figure 2b). The energy values are more variable, and the mean energy is larger. It is suggested that significant further energization of the ring current occurs during the sequence of compound substorms (as  $n_s$  increases). For the following analysis, we choose to focus only on isolated substorms and the first compound substorm of a sequence (hereafter referred to simply as a compound substorm). This will reduce the clear variability observed within a series of compound substorms and avoid the effects of preconditioning on the observed energy values.

Figures 2d, 2e, 3d, and 3e show how the Kolmogorov-Smirnov test can be applied to identify statistically significant differences in the energy distributions, in this case comparing the energy distributions during the growth phase to the expansion phase. From the cumulative probability distributions shown in Figures 2d and 2e, the energy bin associated with the maximum absolute difference between the distributions is identified. The magnitude of the difference, shown by the blue arrows, provides the value of the Kolmogorov-Smirnov test statistic. The corresponding  $p$  values from the Kolmogorov-Smirnov test indicate the probability that the distributions are drawn from the same population. Comparing the growth phase to the expansion phase for  $H^+$  ions, the  $p$  value for isolated substorms is  $9.7 \times 10^{-3}$  and the  $p$  value for compound substorms with  $n_s = 0$  is  $6.0 \times 10^{-3}$ . Using a typical probability threshold of 0.01, we can identify that the energy distributions for the growth and expansion phases have statistically significant differences. For the  $O^+$  ions (Figures 3d and 3e), the  $p$  values are 0.11 for isolated substorms and 0.01 for compound substorms with  $n_s = 0$ . Therefore, for  $O^+$  ions in this spatial bin, the growth and expansion phase distributions are not identified to be statistically significantly different for the isolated substorms and the difference is marginal for the compound substorms.

Whereas Figures 2 and 3 focus on one spatial bin, we also extend the analysis to assess the global distribution of energy values for both isolated and compound substorms. Figures 4 and 5 show mean energy values for all L-MLT bins, for the  $H^+$  and  $O^+$  ions, respectively. The mean energies are shown for the isolated substorms during the (a) growth and (b) expansion phases. The corresponding values for the compound substorms during the (d) growth and (e) expansion phases are also shown. The number of samples in each L-MLT bin (provided in Figure S1 of the supporting information) shows that the number of values in a given L-MLT bin ranges from more than 50 to several hundred samples, which is sufficient for the statistical

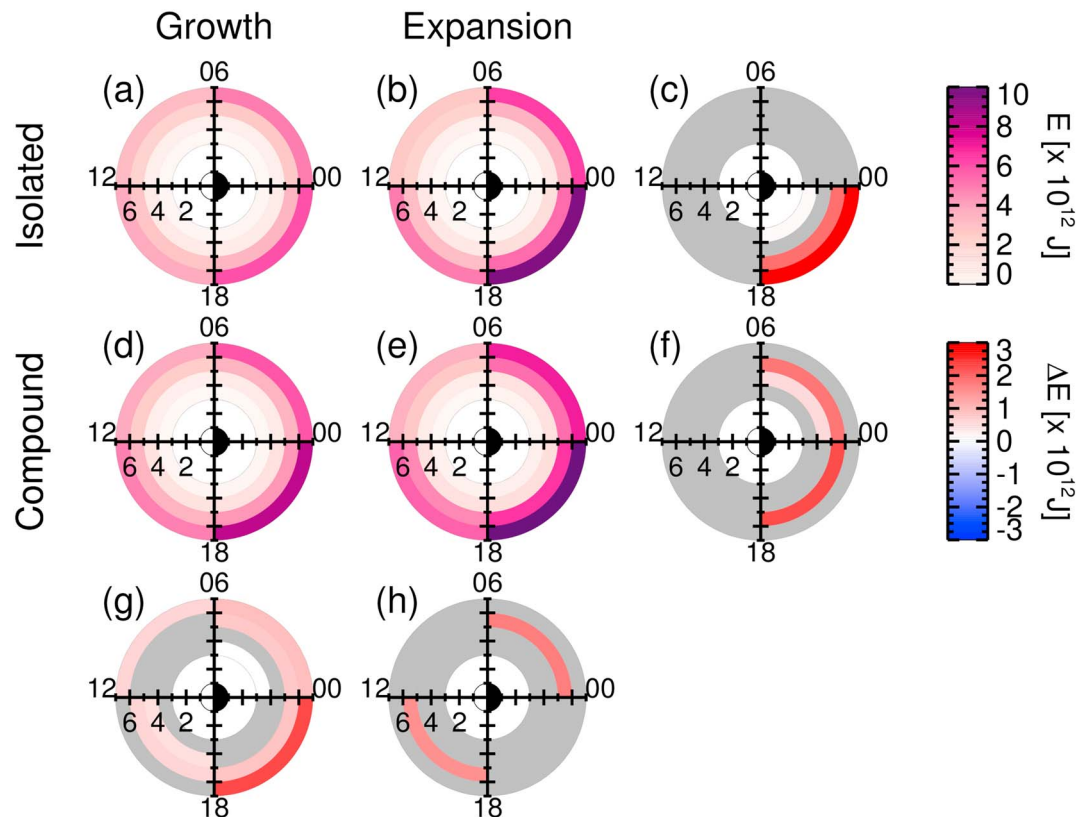


**Figure 4.** Values for each L-MLT bin are plotted at the bins' location in the L-MLT domain for the  $H^+$  ions. The mean energy values,  $E$  (J), are shown for (a) growth phases of isolated substorms, (b) expansion phases of isolated substorms, (d) growth phases of compound substorms, and (e) expansion phases of isolated substorms. The difference in the mean values,  $\Delta E$  (J), for the expansion phase relative to the growth phase is shown for (c) isolated substorms and (f) compound substorms. The difference in mean values for the compound substorms relative to the isolated substorms is shown for (g) the growth phase and (h) the expansion phase. It is noted that, for the difference plots (c, f, g, h), the difference in mean values is only plotted if the distributions are identified to be statistically different according to the Kolmogorov-Smirnov test with  $p < 0.01$ . MLT = magnetic local time.

analysis conducted here. To compare the change in mean energy from the growth to the expansion phase, the difference in mean energies for the expansion phase relative to the growth phase is shown for (c) isolated substorms and (f) compound substorms. For a given L-MLT bin, the distribution of values in the growth and expansion phase is compared under the Kolmogorov-Smirnov test, as described above. If the  $p$  value is less than 0.01, then the distributions are shown to be significantly different, and the difference in the mean values is plotted. If  $p \geq 0.01$ , there is no significant difference in the distributions and the bin is plotted as light gray. Using the same approach, we also compare the mean values between isolated and compound substorms during the (g) growth and (h) expansion phases. The use of the Kolmogorov-Smirnov testing allows us to identify the L-MLT bins that are associated with statistically significant changes in the mean energy over onset (c, f) and statistically significant differences with substorm type (g, h).

The spatial distributions shown in Figures 4 and 5 are qualitatively similar. The  $L$  dependence observed is such that the energy values increase with  $L$ , which is a consequence of the approach used. The volume corresponding to the L-MLT bin, over which the energy density is integrated over, increases with  $L$  value. Figures 4 and 5 also show that the energy values have a clear azimuthal asymmetry, such that the energy values tend to be greatest in the premidnight MLT sector.

The magnitudes of the energy values differ for the  $H^+$  and  $O^+$  ions, as expected based on previous work (Sandhu et al., 2018), where this feature was also identified from Figures 2 and 3. The mean energy value for an L-MLT bin extends up to  $\sim 10^{13}$  J for the  $H^+$  ions, whereas for the  $O^+$  ions the value ranges up to  $\sim 3 \times 10^{12}$  J.

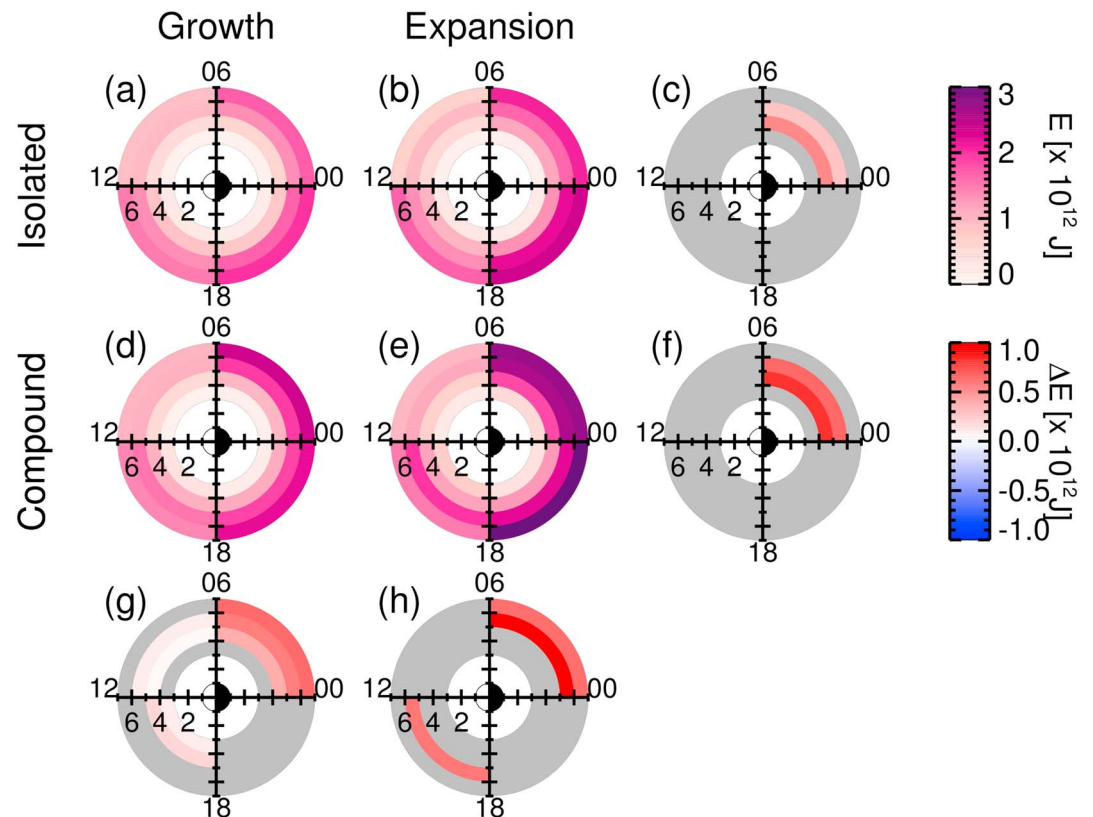


**Figure 5.** Following the same format as Figure 4 for the  $O^+$  ions.

For a given ion species, differences and changes in the mean energy with substorm type as well as from the growth to expansion phase of a substorm are apparent and are quantitatively demonstrated by the  $\Delta E$  L-MLT maps. Figures 4c and 4f show that, for both isolated and compound substorms, the only statistically significant changes in the energy content following substorm onset are enhancements that occur on the nightside region. The enhancements are of the order of  $10^{12}$  J in magnitude and are largest in the premidnight MLT sector. The magnitude of the changes are comparable between the isolated and compound substorms. The corresponding changes in energy content following substorm onset for the  $O^+$  ions are shown in Figures 5c and 5f. Similar to the  $H^+$  ions, an enhancement in energy content is observed. The enhancement is localized to the postmidnight MLT sector and is of the order  $10^{11}$  J.

The differences in ring current energy content during isolated and compound substorms can also be identified. Figures 4g and 4h show that the mean  $H^+$  energy content tends to be greater during compound substorms than during isolated substorms, both before and after substorm onset. The difference in energy values ( $\sim 10^{12}$  J) is comparable to the magnitudes of postonset changes (Figures 4c and 4f). During the growth phase, the statistically significant differences in energy content between isolated and compound substorms spans over all MLT sectors (Figure 4g). In contrast, during the expansion phase, the differences are reduced and occur only in the postmidnight and afternoon MLT sectors (Figure 4h). The corresponding results for the  $O^+$  ions show similar trends (Figures 5g and 5h). The energy content of  $O^+$  ions is consistently larger during compound substorms compared to isolated substorms, both in the growth phase and expansion phase of the substorms. The magnitude of the energy difference is  $\sim 10^{12}$  J, and a comparison to Figures 5c and 5f indicates that the differences between isolated and compound substorms are larger than the changes in energy content following substorm onset. In terms of the spatial distribution of significant enhancements in Figure 5, the  $O^+$  ions show similar trends to those observed for  $H^+$  ions.

It is also useful to consider the global energy content from each ion species in this energy range. We estimate this by summing the mean values from each L-MLT bin in a given L-MLT map, in the same manner as Sandhu et al. (2018). Table 1 shows the estimated global energy content for the  $H^+$  and  $O^+$  ions for the growth phase and expansion phase of both isolated and compound substorms. The differences in global

**Table 1**  
Global Energy Content ( $\times 10^{13}$  J) for  $H^+$  ( $O^+$ ) Ions

Substorm category	Growth	Expansion	Expansion-growth
Isolated	3.3 (1.5)	4.3 (1.8)	1.0 (0.3)
Compound	4.2 (1.8)	5.7 (2.3)	1.5 (0.5)
Compound-isolated	0.9 (0.3)	1.4 (0.5)	

energy content for the expansion phase relative to the growth phase are also shown, as well as differences for compound substorms relative to isolated substorms. Table 1 provides an indication of how much energy the  $H^+$  and  $O^+$  ions with energies 1 eV to 50 keV contribute to the total ring current energy. Table 1 shows that the global energy content for both  $H^+$  and  $O^+$  ions is  $\sim 10^{13}$  J, and the values are larger for the  $H^+$  ions. As expected from Figures 4 and 5, the average energy content increases following substorm onset, and the enhancement is greater for compound substorms compared to isolated substorms. The global energy content is larger for compound substorms compared to isolated substorms, during both the growth and expansion phases.

#### 4. Substorm Characteristics

In order to understand the clear and significant differences in ring current energy content and response to onset for isolated substorms compared to compound substorms, we consider substorm properties and background conditions. In Figure 6, a superposed epoch analysis of various parameters is shown, relative to substorm onset time, for the substorms considered in this study. The mean values are shown for 5 min time bins for a time window spanning 60 min before onset to 60 min after onset. The pale pink lines correspond to isolated substorms, and the dark purple lines correspond to compound substorms. Figure 6a shows the average values of the SML index (nT). The SML index is an indicator of the nightside auroral electrojet activity and a depression of the SML index following substorm onset is an indicator of the substorm size (Newell & Gjerloev, 2011). Prior to onset the SML index is consistently decreased for compound substorms compared to isolated substorms by approximately 15 nT. This is indicative of enhanced convection as well as prior substorm activity. Figure 6a demonstrates that the change in SML index following onset is greater for compound substorms compared to isolated substorms, by approximately 20 nT. Following the rapid reduction in SML index associated with the substorm expansion phase (lasting approximately 25 min on average from Figure 6a), it can be seen that the isolated substorms demonstrate a gradual increase in SML index, which is a typical feature of the substorm recovery phase. In contrast, the compound substorms show that the SML index remains at a depressed level. This feature is due to the averaging of successive expansion phases following the first substorm in the series.

Figure 6b shows the average values of the dayside reconnection electric field,  $E_R$  (mV/m). For a given time bin of a given substorm, the dayside reconnection electric field is estimated from

$$E_R = V_x B_{yz} \sin^2 \left( \frac{\theta}{2} \right) \quad (3)$$

where  $V_x$  is the Geocentric Solar Magnetic  $x$  component of the solar wind speed,  $B_{yz}$  is the IMF component in the Geocentric Solar Magnetic  $y$ - $z$  plane, and  $\theta$  is the IMF clock angle (Kan & Lee, 1979). The dayside reconnection electric field provides an indication of the rate of low-latitude reconnection on the dayside magnetopause. An elevated dayside reconnection electric field corresponds to increased loading of the magnetotail with open flux and increased convection in the magnetosphere (Dungey, 1961; Milan et al., 2003, 2007). The enhanced driving is also associated with increased geomagnetic activity including substorm occurrences (e.g., Fairfield & Cahill, 1966). Figure 6 shows that the average magnitude of the dayside reconnection electric field is greater for compound substorms compared to isolated substorms by more than 30% at substorm onset. The magnitude remains markedly greater for compound substorms both before and after substorm onset.

Furthermore, we also show the average value of the Sym-H\* index (nT) in Figure 6. The Sym-H index represents the horizontal magnetic field perturbations as measured by ground magnetometers, where reductions in the Sym-H index are commonly used as indicators of global geomagnetic ring current intensifications (Dessler & Parker, 1959; Sckopke, 1966). As the Sym-H index is known to include contributions from additional current systems (e.g., Burton et al., 1975; Turner et al., 2000), there have been attempts to account for



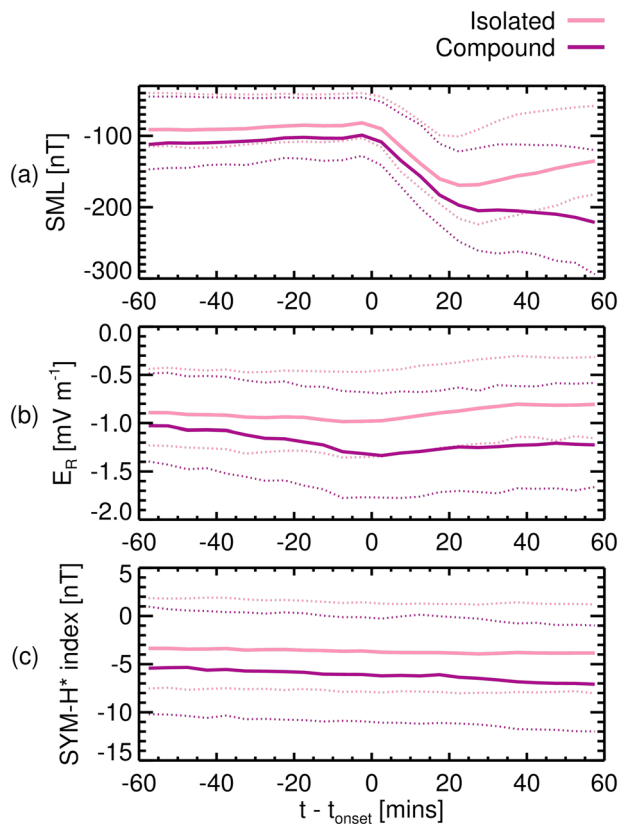


**Figure 6.** Superposed epoch analysis of (a) SML index (nT), (b) dayside reconnection electric field,  $E_R$ , (mV/m), (c) Sym-H\* index (nT). The mean values in 5-min bins are plotted relative to the time of substorm onset for isolated substorms (pale pink) and compound substorms (dark purple). The lower quartiles and upper quartiles are shown by the thin dotted lines.

these additional contributions through a corrected index, known as the Sym-H\* index (e.g., Burton et al., 1975; Gonzalez et al., 1994). Here we opt to use the Gonzalez et al. (1994) definition of the Sym-H\* index, in order to more accurately describe the ring current magnitude and variations. Consistent with the low-energy ion observations presented in section 3, it is observed that the magnitude of the Sym-H\* index is, on average, greater for compound substorms compared to isolated substorms. We note that the Sym-H\* index includes contributions across all ion energy ranges and species, and the magnitude of the Sym-H\* index is dominated by protons with energies of hundreds of kiloelectron volts. Overall, we observe differences in the SML index, the  $E_R$  parameter, and the Sym-H\* index prior to onset. It can be observed that these differences persist for multiple days prior to onset (shown in Figure S2 of the supporting information), suggesting substantially different time histories associated with isolated and compound substorms.

In addition, we have the distributions of the duration of the substorm growth and expansion phases and of the onset latitude and MLT. We find that the growth phase duration exhibits statistically significant differences ( $p$  value of  $\sim 10^{-6}$  under the Kolmogorov-Smirnov test), such that isolated substorms typically have a longer growth phase. The mean duration of a growth phase is 249 min for isolated substorms and 187 min for compound substorms. Furthermore, statistically significant differences are also observed for the expansion phase duration ( $p$  value of 0.002). Compound substorms tend to have longer expansion phase durations compared to isolated substorms, with mean durations of 25 and 28 min, respectively.

It is also observed that the distribution of onset latitudes was different ( $p$  value of  $\sim 10^{-4}$ ), such that isolated substorms onsets tend to occur at higher invariant latitudes. In contrast, the MLT of onsets was not significantly different for isolated substorms compared to compound substorms ( $p$  value of 0.12). The results of this assessment are included in Figures S3 and S4 of the supporting information.

## 5. Discussion

The results presented in section 3 indicate statistically significant variations in the low-energy ion population of the ring current, for both  $H^+$  and  $O^+$  ions, during the substorm process. It has been clearly identified that the energy contributed by the ions differs for compound substorms compared to isolated substorms, both before and after substorm onset. We establish that the compound substorms are associated with larger energy content values before and after substorm onset and that the postonset energization is larger for compound substorms than isolated substorms. Furthermore, an examination of the average substorm properties and solar wind magnetosphere coupling indicates a prolonged higher level of dayside coupling during compound substorms. Compound substorms are also larger than isolated substorms, on average. We will now discuss the implications of these findings and explore the drivers of the observed differences.

### 5.1. Enhancements Following Substorm Onset

Figures 4c, 4f, 5c, and 5f demonstrate a statistically significant increase in the mean energy values following substorm onset, although there are some variations between the ion species. In terms of the  $H^+$  ions, Figures 4c and 4f show that the enhancement following substorm onset is largely in the premidnight MLT sector, consistent with the results of Sandhu et al. (2018). Previous studies have identified that substorm injections of particles occur across the nightside MLT sector (Reeves et al., 1990, 1991, 1992), although there is a preference for the premidnight MLT sector compared to the postmidnight MLT sector (e.g., Gabrielse et al., 2014; Kokubun & McPherron, 1981; Sarris et al., 1976). The injected ion population then experience a westward drift in the inner magnetosphere (Lopez et al., 1990; Mauk & McIlwain, 1974; McIlwain, 1974;

Reeves et al., 1990). The combination of the injection occurrence MLT distribution and the duskward transport of injected  $H^+$  ions produces the significant enhancement in the premidnight MLT sector.

Figures 5c and 5f show that the postonset enhancement in energy content from the  $O^+$  ions is localized to the postmidnight sector, in contrast to the result from the  $H^+$  ions. It is unclear why the composition of the plasma would affect the local time preference of the injection, such that  $O^+$  ions are more likely to be injected in the postmidnight MLT sector compared to the premidnight MLT sector. One potential reason may be deduced from the drift paths of the  $O^+$  ions following injection. For ions with sufficient energy, the gradient-curvature drift is dominant and the ions drift westward through the dusk sector. However, if the energy of the  $O^+$  ions is low such that the convection electric field dominates the drift path, the ions will be convected through the dawn sector (Ozeke & Mann, 2001). However, there is no clear evidence that  $O^+$  ions typically have a lower characteristic energy in the inner magnetosphere than  $H^+$  ions. The cause of the  $O^+$  dawn enhancement remains unknown, and it is highlighted that this feature is certainly worthy of future investigation.

### 5.2. What Are the Differences Between Isolated and Compound Substorms?

The results highlighted several key differences in the ring current energy content between isolated and compound substorms, which can be summarized as

1. The energy content is enhanced, both before and after substorm onset, for compound substorms compared to isolated substorms (Figures 4g, 4h, 5g, and 5h). The global energy content contributed by low-energy  $H^+$  and  $O^+$  ions is larger during compound substorms than isolated substorms, by  $\sim 20\text{--}30\%$  (Table 1).
2. For both the  $H^+$  and  $O^+$  ions, the energy content is more localized to the premidnight MLT sector for isolated substorms, whereas the energy is elevated across a more azimuthally extensive area for compound substorms (Figures 4g, 4h, 5g, and 5h).
3. Compound substorms are associated with larger enhancements following substorm onset than isolated substorms (Figures 4c, 4f, 5c, and 5f and Table 1). The compound substorms are also associated with larger relative changes in energy content over onset. For example, the energy content is enhanced by 30% for isolated substorms and by 40% for compound substorms for  $H^+$  ions, with similar trends observed for  $O^+$  ions.
4. The postonset enhancements extend across both nightside MLT sectors for compound substorms but are localized solely to the premidnight MLT sector for isolated substorms (Figures 4c, 4f, 5c, and 5f).

We will now discuss how the magnetospheric conditions and time history can impart these observed differences between isolated and compound substorms.

Previous work has strongly established that enhanced dayside driving and nightside auroral activity, as observed for the compound substorms from Figures 6a and 6b, results in enhanced ionospheric outflows of both  $H^+$  and  $O^+$  ions (Axford, 1968; Lockwood et al., 1985, 1985; Yau & Andre, 1997). Through convection, the outflows are transported to both the plasma sheet and inner magnetosphere, increasing the hot plasma density and energy (Haaland et al., 2009; Kistler et al., 2010; Kozyra & Liemohn, 2003; Wang et al., 2006; Winglee, 2000). In terms of the convective transport of plasma to the ring current, the greater level of solar wind-magnetosphere coupling during compound substorms corresponds to increased convection (Cowley, 1981), suggesting more efficient transport of ions into and across the inner magnetosphere. As well as increasing the density of the ring current, this allows the ions to populate a wider range of MLT sectors during compound substorms than isolated substorms. Furthermore, the convective drifts are more likely to dominate over the gradient-curvature drifts and the ions will be effectively transported to the postmidnight sector as well as to the dayside. In contrast, during isolated substorms, where the convection is relatively (Ozeke & Mann, 2001) stagnated, ions are less effectively transported throughout the magnetosphere and the energy content is more azimuthally localized. It is highlighted that the relatively active geomagnetic conditions associated with the compound substorms compared to the isolated substorms are maintained for approximately days prior to onset, allowing significant differences in the ring current and plasma sheet populations to develop.

The enhanced density and energy of the plasma sheet during compound substorms are corresponded in the injected population following substorm onset. Compound substorms are also, on average, larger than isolated substorms (Figure 6a). Larger substorms are associated with a greater level of dipolarization in the inner magnetosphere, which increases the energization of particles as they are transported inward

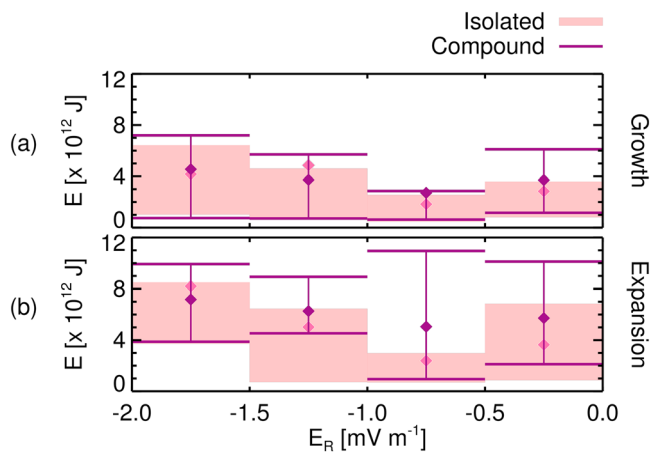


**Figure 7.** The mean  $H^+$  energy content,  $E$  (J), for an L-MLT bin covering  $5 \leq L < 6$  and  $18 \leq MLT < 24$  is indicated by the diamonds, and the bars/shaded region shows the extent of the lower quartile to the upper quartile. Values during the (a) growth phase and (b) expansion phase are shown. Values corresponding to isolated substorms are shown in pink, and values corresponding to compound substorms are shown in purple. The energy content values are binned for the estimated dayside reconnection electric field,  $E_R$  (mV/m), at substorm onset, as labeled on the x axis.

(Aggson et al., 1983; Ashour-Abdalla et al., 2009; Nakamura et al., 2017; Quinn & Southwood, 1982; Zaharia et al., 2000). This results in a higher density of ions injected to the inner magnetosphere, with higher energies, for compound substorms compared to isolated substorms. Furthermore, Reeves and Henderson (2001) showed that substorms associated with continued injections demonstrated a spatial broadening of the injection region following onset, such that it was able to extend azimuthally across the full nightside MLT sector. The broader injection region associated with compound substorms would act to increase the energy content in the postmidnight MLT sector compared to isolated substorms, in agreement with the observations.

Overall, both the convective and impulsive supply of ions to the ring current following substorm onset are more effective for compound substorms, resulting in the observed larger and more spatially extensive postonset energization. Furthermore, we also note that the occurrence of the first compound substorm in a sequence will drive further enhancements of ionospheric outflows, thus magnifying the ring current energization for the subsequent substorms that follow.

Previous studies have also shown that enhanced outflows are associated with an enhanced concentration of  $O^+$  ions in the plasma sheet and the inner magnetosphere (e.g., Maggiolo & Kistler, 2014; Sandhu et al., 2016, 2017). Although we are not examining the densities in this study, a consideration of the  $H^+/O^+$  energy content ratio indicates no clear variations

(the ratio ranges between 0.41 and 0.45, both before and after onset and for isolated and compound substorms). We suggest that, as the estimated energy content depends on the ion energy as well as the fluxes, the variations in energy content are more complex than densities.

As well as differences in the solar wind coupling and substorm size, the inner magnetospheric conditions prior to onset may also be important in determining the magnitude of the energy content enhancement. It has been suggested that a large magnetic field gradient from the plasma sheet to the inner magnetosphere can act to divert flows before the plasma can be transported to the inner magnetosphere (Sergeev et al., 2012; Takada et al., 2006). The magnetic field perturbation associated with the ring current is southward in the inner magnetosphere and northward in the outer region. This acts to weaken and reduce the radial gradient in the background magnetic field and therefore increase the probability of an injection in the ring current region. Figure 6c shows the Sym- $H^*$  index, which is a measure of magnetic field perturbations for field lines mapping to the inner magnetosphere, often assumed to arise from the magnetic field contribution from the ring current population (Dessler & Parker, 1959; Sckopke, 1966). As shown by Figure 6c, the compound substorms are associated with a consistently depressed inner magnetospheric field in comparison to isolated substorms and it is proposed that the weaker inner magnetosphere can aid in the accessibility of substorm injections to the inner magnetosphere. Previous work has shown that not all substorms are associated with an observed injection in the inner magnetosphere, with a classical injection occurrence probability of  $\sim 30\%$  (Boakes et al., 2011). We suggest that the weaker inner magnetospheric field associated with compound substorms compared to isolated substorms acts to increase the probability of an injection to the ring current region. On average, this contributes to the observed difference in the magnitude of postonset energization.

### 5.3. Parameterizing Ring Current Energy Content by Solar Wind Driving

The key differences in energy content between isolated and compound substorms have largely been attributed to the prolonged differing solar wind-magnetosphere coupling (Figure 6b), which drives ionospheric outflows, substorm activity, and transport of plasma to the inner magnetosphere. We now examine whether the different average solar wind driving is the key factor in shaping the ring current energy content for the low-energy ions. Specifically, we address whether an isolated substorm associated with the same level of solar wind driving as a compound substorm will have the same energy content value. It is noted here that the level of solar wind driving is prolonged for days prior to onset (Figure S2 in the supporting information). However, here we opt to simply use the value of  $E_R$  at onset, which is expected to correspond to a sustained prior driving at that level beforehand and correspond to substorms with a similar time history.

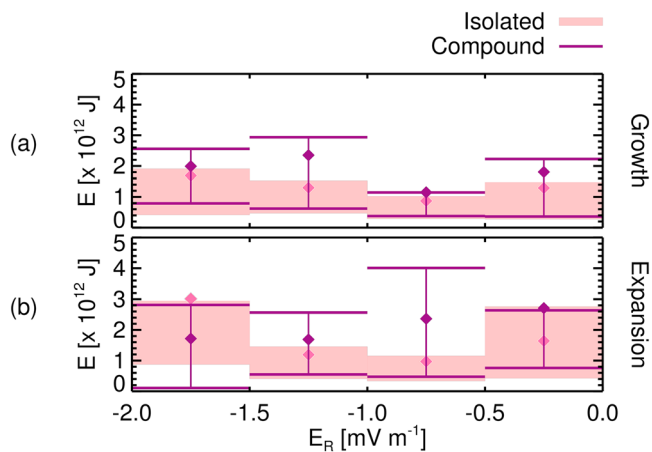


**Figure 8.** Following the same format as Figure 7 for the  $O^+$  ions in a spatial bin covering  $5 \leq L < 6$  and  $00 \leq MLT < 06$ .

Figures 7 and 8 show the mean energy content during the (a) growth and (b) expansion phases. The energy values are binned for the estimated dayside reconnection electric field,  $E_R$  (mV/m), at substorm onset, therefore restricting the values to substorms with the same level of solar wind driving. The pink diamonds represent the mean value for isolated substorms, and the purple diamonds represent the mean value for compound substorms. The bars indicate the extent of the upper and lower quartiles, using the same color coding. Figure 7 shows results for the  $H^+$  ions for an L-MLT bin located in the premidnight MLT sector, and Figure 8 corresponds to  $O^+$  ions for an L-MLT bin in the postmidnight MLT sector. The location of the bins was selected to correspond to the L-MLT location of the largest enhancements observed in Figures 4 and 5.

Figures 7 and 8 indicate that the mean energy content (in a given phase for a given  $E_R$  bin) is similar between isolated and compound substorms, relative to the spread of values indicated by the quartiles. Conducting Kolmogorov-Smirnov statistical testing demonstrates that there are no statistically significant differences between the energy distributions associated with isolated and compound substorms, for any of the bins shown.

In addition, it can be seen that the spread of values (indicated by the width of the bars in Figures 7 and 8) generally tends to be greater for compound substorms compared to isolated substorms and in particular that the upper quartile extends to higher values. This feature suggests that the tail of the energy distributions for compound substorms is larger compared to isolated substorms, consistent with Figures 2 and 3.

The results suggest that the ring current energy content, both before and after onset, is largely controlled by the level of solar wind driving and that the magnitude of solar wind-magnetosphere coupling is the main contributor of variations between isolated and compound substorms. Furthermore, we observe a weak correlation between the solar wind driving and the substorm size (a Pearson's linear correlation coefficient of up to 0.2 with a significance of  $10^{-17}$ ), providing some support to observations that the solar wind driving controls substorm intensity (e.g., Li et al., 2013). Therefore, we suggest that the physics of isolated and compound substorms are essentially the same, but that the properties of the two types of substorm (e.g., substorm size shown by the SML index) and the ring current evolution associated with them differ because of different solar wind magnetosphere coupling that occurs on timescales of days. The more prolonged coupling during compound substorms imparts significant differences in the ring current energy content preceding substorm onset and in the postonset energization.

#### 5.4. The Influence of the Ring Current on Compound Substorms

The analysis presented in section 3 demonstrates clear differences in the preonset conditions associated with isolated and compound substorms. Although it is currently unclear why a series of compound substorms may occur as opposed to an isolated substorm, the results presented here may provide some insight into the role of inner magnetospheric conditions in shaping the properties of compound substorms.

Figures 6b and 6c clearly demonstrate that compound substorms are associated with higher driving and an enhanced ring current before substorm onset, as previously discussed. It has been suggested that these conditions are favorable to more intense substorms initiated at field lines that map to low magnetic latitudes in the ionosphere (Milan, 2009; Milan et al., 2008; Milan, Grocott, et al., 2009; Milan, Hutchinson, et al., 2009; Nakai & Kamide, 2003). This is due to a feedback mechanism where the induced magnetic field from the ring current introduces a significant northward component in the tail, acting to reduce tail stretching and stabilize the tail to onset. Therefore, the magnetosphere requires more open flux to accumulate in the tail (driving the auroral oval to lower latitudes) in order to reach conditions favorable for substorm onset. As these substorms are initiated at lower latitudes, the amount of open flux closed is larger and the substorm is more intense (Akasofu, 1975; Kamide et al., 1999; Milan, Grocott, et al., 2009). Therefore, as the compound substorms assessed here are associated with an enhanced ring current prior to onset (Figures 4g, 5g, and 6c) compared to isolated substorms, the events are more intense and result in larger postonset ion energization.

Whereas Milan et al. (2008) observed the onset latitudes from auroral observations (see also Milan, Grocott, et al., 2009; Milan, Hutchinson, et al., 2009; Milan, 2009), the SOPHIE technique can be used here to identify the magnetic latitude and local time of the active ground magnetometer station that observes the

substorm-associated SML signature. The results are included in Figure S4 of the supporting information and we find that, in contrast to the feedback mechanism, the compound substorm onsets do not occur at a significantly lower invariant latitude than for isolated substorms. It is highlighted that further investigation is required to fully understand how the use of a different onset identification technique may introduce differences. Furthermore, the feedback mechanism was developed to correspond to observations that included storm time ring current conditions, where the ring current is significantly more enhanced than the observations presented in this study. Therefore, we suggest that larger enhancements in the ring current than are observed here are required for significant deviations in the onset latitude to be present.

Continuing the comparison to the results of Milan et al. (2008), Milan, Grocott, et al. (2009), Milan, Hutchinson, et al. (2009), and Milan (2009), we observe that a continued high level of solar wind driving is observed following onset for compound substorms, whereas the driving subsides for isolated substorms (Figure 6b). The high level of solar wind driving following the onset of the first compound substorm is thought to efficiently load the magnetotail with open flux, allowing the tail to reach a state favorable to onset relatively rapidly. Therefore, the magnetosphere can reach an “onset ready” condition during the recovery phase, resulting in a compound event to occur. However, we note that the physical processes responsible for substorm onset are well debated (e.g., Angelopoulos et al., 2008; Baker et al., 1996; Kalmoni et al., 2015; Lui et al., 1991, 2009) and that a fuller understanding of how substorms are initiated is required to establish why compound substorms occur instead of isolated substorms.

## 6. Conclusions

An analysis of HOPE H<sup>+</sup> and O<sup>+</sup> ion observations (1 eV to 50 keV) in the growth and expansion phases of substorms was conducted to quantitatively identify differences in energy content during isolated and compound substorms. We establish that the energy content associated with the ions is significantly increased following substorm onset for both isolated and compound substorms, where the local time of the enhancements provide insight into the drift paths of injected H<sup>+</sup> and O<sup>+</sup> ions in the inner magnetosphere.

A comparison of isolated and compound substorms demonstrates clear differences in the corresponding ring current energy content. Quantitative estimates of the energy content and differences are provided. In addition, we demonstrate the statistical significance of the differences in energy content over onset and comparing isolated and compound substorms. It is observed that compound substorms are associated with an enhanced ring current on average, both before and after onset, relative to isolated substorms. Furthermore, compound substorms are associated with a larger energy input following onset than isolated substorms. A consideration of the average solar wind-magnetosphere coupling, substorm size, and inner magnetospheric conditions provides context on how differences between isolated and compound substorms arise. Stronger ionospheric outflows, more effective circulation of plasma, larger magnitude of dipolarization, and increased accessibility of injections to the inner magnetosphere are highlighted as the key factors contributing to the difference in compound substorms relative to isolated substorms. In addition, we establish that the difference in average solar wind coupling is a significant source of variability for the ring current conditions.

Overall, we have demonstrated that there are significant differences between isolated and compound substorms, in terms of the ring current state and substorm-associated energization. It has been found that a single compound substorm is more effective at energizing the ring current than an isolated substorm. We highlight that this study considered only the first compound substorm for each series of compound substorms in an event. Therefore, we can expect that the combined sequence would be highly effective at energizing the ring current to generate a strongly enhanced ring current compared to inactive geomagnetic conditions. It is reasonable to assume that the successive substorms in the event would have similar energy inputs to the ring current region based on the continued strong solar wind driving, although a full consideration of the impacts of the whole compound event is left to a future study.

## References

- Aggson, T. L., Heppner, J. P., & Maynard, N. C. (1983). Observations of large magnetospheric electric fields during the onset phase of a substorm. *Journal of Geophysical Research*, *88*(A5), 3981–3990. Retrieved from <https://doi.org/10.1029/JA088iA05p03981>
- Akasofu, S.-I. (1968). The growth of the storm-time radiation belt and the magnetospheric substorm. *Geophysical Journal of the Royal Astronomical Society*, *15*(1-2), 7–21. Retrieved from <https://doi.org/10.1111/j.1365-246X.1968.tb05741.x>

### Acknowledgments

J. K. S. is supported by STFC grant ST/N000722/1 and NERC Grant NE/P017185/1, I. J. R. is supported by STFC Grant ST/N000722/1 and NERC Grant NE/P017185/1, C. F. is supported by NERC IRFNE/N014480/1, K. R. M. is supported by NSF Grant 1602403 and NASA Grants 18-HGIO18\_2-012 and 18-HSWO2R18-0010, and M. -T. W. is supported by NERC Grant NE/P001556/1. Processing and analysis of the HOPE data were supported by Energetic Particle, Composition, and Thermal Plasma (RBSP-ECT) investigation funded under NASAs Prime contract NAS5-01072. All RBSP-ECT data are publicly available at the Web site (<http://www.RBSP-ect.lanl.gov/>). The SML index data are publicly available online (<http://supermag.jhuapl.edu>). We gratefully acknowledge the SuperMAG collaborators (<http://supermag.jhuapl.edu/info/?page=acknowledgement>). The solar wind data and Sym-H index data are publicly available online (<http://wdc.kugi.kyoto-u.ac.jp/index.html>).

- Akasofu, S.-I. (1975). The roles of the north-south component of the interplanetary magnetic field on large-scale auroral dynamics observed by the DMSP satellite. *Planetary and Space Science*, 23(10), 1349–1354. Retrieved from [https://doi.org/10.1016/0032-0633\(75\)90030-6](https://doi.org/10.1016/0032-0633(75)90030-6)
- Akasofu, S.-I., Chapman, S., & Venkatesan, D. (1963). The main phase of great magnetic storms. *Journal of Geophysical Research*, 68(11), 3345–3350. Retrieved from <https://doi.org/10.1029/JZ068i011p03345>
- Angelopoulos, V., McFadden, J. P., Larson, D., Carlson, C. W., Mende, S. B., Frey, H., et al. (2008). Tail reconnection triggering substorm onset. *Science*, 321(5891), 931–935. Retrieved from <https://doi.org/10.1126/science.1160495>
- Ashour-Abdalla, M., Bosqued, J.-M., El-Alaoui, M., Perroomian, V., Zhou, M., Richard, R., et al. (2009). A simulation study of particle energization observed by THEMIS spacecraft during a substorm. *Journal of Geophysical Research*, 114, A09204. Retrieved from <https://doi.org/10.1029/2009JA014126>
- Axford, W. I. (1968). The polar wind and the terrestrial helium budget. *Journal of Geophysical Research*, 73, 6855–6859. <https://doi.org/10.1029/JA073i021p06855>
- Baker, D. N., Pulkkinen, T. I., Angelopoulos, V., Baumjohann, W., & McPherron, R. L. (1996). Neutral line model of substorms: Past results and present view. *Journal of Geophysical Research*, 101, 12,975–13,010. <https://doi.org/10.1029/95JA03753>
- Boakes, P. D., Milan, S. E., Abel, G. A., Freeman, M. P., Chisham, G., & Hubert, B. (2011). A superposed epoch investigation of the relation between magnetospheric solar wind driving and substorm dynamics with geosynchronous particle injection signatures. *Journal of Geophysical Research*, 116, A01214. Retrieved from <https://doi.org/10.1029/2010JA016007>
- Burton, R. K., McPherron, R. L., & Russell, C. T. (1975). An empirical relationship between interplanetary conditions and dst. *Journal of Geophysical Research*, 80(31), 4204–4214. Retrieved from <https://doi.org/10.1029/JA080i031p04204>
- Cowley, S. (1981). Magnetospheric and ionospheric flow and the interplanetary magnetic field.
- Daglis, I. A., Thorne, R. M., Baumjohann, W., & Orsini, S. (1999). The terrestrial ring current: Origin, formation, and decay. *Reviews of Geophysics*, 37(4), 407–438. Retrieved from <https://doi.org/10.1029/1999RG900009>
- Dessler, A. J., & Parker, E. N. (1959). Hydromagnetic theory of geomagnetic storms. *Journal of Geophysical Research*, 64(12), 2239–2252. Retrieved from <https://doi.org/10.1029/JZ064i012p02239>
- Dungey, J. W. (1961). Interplanetary magnetic field and the auroral zones. *Physical Review Letters*, 6, 47–48. Retrieved from <https://doi.org/10.1103/PhysRevLett.6.47>
- Fairfield, D. H., & Cahill, L. J. Jr. (1966). Transition region magnetic field and polar magnetic disturbances. *Journal of Geophysical Research*, 71(1), 155–169. Retrieved from <https://doi.org/10.1029/JZ071i001p0155>
- Forsyth, C., Rae, I. J., Coxon, J. C., Freeman, M. P., Jackman, C. M., Gjerloev, J., & Fazakerley, A. N. (2015). A new technique for determining substorm onsets and phases from indices of the electrojet (SOPHIE). *Journal of Geophysical Research: Space Physics*, 120, 10,592–10,606. Retrieved from <https://doi.org/10.1002/2015JA021343>
- Forsyth, C., Watt, C. E. J., Rae, I. J., Fazakerley, A. N., Kalmoni, N. M. E., Freeman, M. P., et al. (2014). Increases in plasma sheet temperature with solar wind driving during substorm growth phases. *Geophysical Research Letters*, 41, 8713–8721. Retrieved from <https://doi.org/10.1002/2014GL062400>
- Funsten, H. O., Skoug, R. M., Guthrie, A. A., MacDonald, E. A., Baldonado, J. R., Harper, R. W., et al. (2013). Helium, oxygen, proton, and electron (HOPE) mass spectrometer for the radiation belt storm probes mission. *Space Science Reviews*, 179(1), 423–484. <https://doi.org/10.1007/s11214-013-9968-7>
- Gabrielse, C., Angelopoulos, V., Runov, A., & Turner, D. L. (2014). Statistical characteristics of particle injections throughout the equatorial magnetotail. *Journal of Geophysical Research: Space Physics*, 119, 2512–2535. Retrieved from <https://doi.org/10.1002/2013JA019638>
- Gjerloev, J. W. (2012). The supermag data processing technique. *Journal of Geophysical Research*, 117, A09213. Retrieved from <https://doi.org/10.1029/2012JA017683>
- Gkioulidou, M., Ukhorskiy, A. Y., Mitchell, D. G., & Lanzerotti, L. J. (2016). Storm time dynamics of ring current protons: Implications for the long-term energy budget in the inner magnetosphere. *Geophysical Research Letters*, 43, 4736–4744. Retrieved from <https://doi.org/10.1002/2016GL068013>
- Gonzalez, W. D., Joselyn, J. A., Kamide, Y., Kroehl, H. W., Rostoker, G., Tsurutani, B. T., & Vasyliunas, V. M. (1994). What is a geomagnetic storm? *Journal of Geophysical Research*, 99(A4), 5771–5792. Retrieved from <https://doi.org/10.1029/93JA02867>
- Haaland, S., Lybekk, B., Svenes, K., Pedersen, A., Förster, M., Vaith, H., & Torbert, R. (2009). Plasma transport in the magnetotail lobes. *Annales Geophysicae*, 27, 3577–3590. <https://doi.org/10.5194/angeo-27-3577-2009>
- Hones, E. W. Jr., & Schindler, K. (1979). Magnetotail plasma flow during substorms: A survey with IMP 6 and IMP 8 satellites. *Journal of Geophysical Research*, 84(A12), 7155–7169. Retrieved from <https://doi.org/10.1029/JA084iA12p07155>
- Hubert, B., Milan, S. E., Grocott, A., Blockx, C., Cowley, S. W. H., & Grard, J.-C. (2006). Dayside and nightside reconnection rates inferred from image FUV and super dual auroral radar network data. *Journal of Geophysical Research*, 111, A03217. Retrieved from <https://doi.org/10.1029/2005JA011140>
- Kalmoni, N. M. E., Rae, I. J., Watt, C. E. J., Murphy, K. R., Forsyth, C., & Owen, C. J. (2015). Statistical characterization of the growth and spatial scales of the substorm onset arc. *Journal of Geophysical Research: Space Physics*, 120, 8503–8516. Retrieved from <https://doi.org/10.1002/2015JA021470>
- Kamide, Y., Kokubun, S., Bargatze, L. F., & Frank, L. A. (1999). The size of the polar cap as an indicator of substorm energy. *Physics and Chemistry of the Earth, Part C: Solar, Terrestrial & Planetary Science*, 24(1), 119–127. Retrieved from <http://www.sciencedirect.com/science/article/pii/S146419179800018X> (International Symposium on Solar-Terrestrial Coupling Processes) [https://doi.org/10.1016/S1464-1917\(98\)00018-X](https://doi.org/10.1016/S1464-1917(98)00018-X)
- Kan, J. R., & Lee, L. C. (1979). Energy coupling function and solar wind-magnetosphere dynamo. *Geophysical Research Letters*, 6(7), 577–580. Retrieved from <https://doi.org/10.1029/GL006i007p00577>
- Kim, H.-J., Lee, D.-Y., & Lyons, L. R. (2008). Are repetitive particle injections during high-speed solar wind streams classic substorms? *Journal of Geophysical Research*, 113, A08205. Retrieved from <https://doi.org/10.1029/2007JA012847>
- Kistler, L. M., Mouikis, C. G., Klecker, B., & Dandouras, I. (2010). Cusp as a source for oxygen in the plasma sheet during geomagnetic storms. *Journal of Geophysical Research*, 115, A03209. <https://doi.org/10.1029/2009JA014838>
- Kokubun, S., & McPherron, R. L. (1981). Substorm signatures at synchronous altitude. *Journal of Geophysical Research*, 86(A13), 11,265–11,277. Retrieved from <https://doi.org/10.1029/JA086iA13p11265>
- Kozyra, J. U., & Liemohn, M. W. (2003). Ring current energy input and decay. *Space Science Reviews*, 109(1), 105–131. Retrieved from <https://doi.org/10.1023/B:SPAC.0000007516.10433.ad>
- Le, G., Russell, C. T., & Takahashi, K. (2004). Morphology of the ring current derived from magnetic field observations. *Annales Geophysicae*, 22(4), 1267–1295. Retrieved from <https://doi.org/10.5194/angeo-22-1267-2004>
- Li, H., Wang, C., & Peng, Z. (2013). Solar wind impacts on growth phase duration and substorm intensity: A statistical approach. *Journal of Geophysical Research: Space Physics*, 118, 4270–4278. Retrieved from <https://doi.org/10.1002/jgra.50399>

- Liou, K., Newell, P. T., Zhang, Y.-L., & Paxton, L. J. (2013). Statistical comparison of isolated and non-isolated auroral substorms. *Journal of Geophysical Research: Space Physics*, *118*, 2466–2477. Retrieved from <https://doi.org/10.1002/jgra.50218>
- Lockwood, M., Waite, J. H., Moore, T. E., Chappell, C. R., & Chandler, M. O. (1985). The cleft ion fountain. *Journal of Geophysical Research*, *90*, 9736–9748. <https://doi.org/10.1029/JA090iA10p09736>
- Lockwood, M., Waite, J. H., Moore, T. E., Chappell, C. R., & Johnson, J. F. E. (1985). A new source of suprathermal  $O^+$  ions near the dayside polar cap boundary. *Journal of Geophysical Research*, *90*, 4099–4116. <https://doi.org/10.1029/JA090iA05p04099>
- Lopez, R. E., Sibeck, D. G., McEntire, R. W., & Krimigis, S. M. (1990). The energetic ion substorm injection boundary. *Journal of Geophysical Research*, *95*(A1), 109–117. Retrieved from <https://doi.org/10.1029/JA095iA01p00109>
- Lui, A. T. Y. (2009). Comment on “tail reconnection triggering substorm onset”. *Science*, *324*(5933), 1391–1391. Retrieved from <https://doi.org/10.1126/science.1167726>
- Lui, A. T. Y., Chang, C.-L., Mankofsky, A., Wong, H.-K., & Winske, D. (1991). A cross-field current instability for substorm expansions. *Journal of Geophysical Research*, *96*(A7), 11,389–11,401. Retrieved from <https://doi.org/10.1029/91JA00892>
- Maggiolo, R., & Kistler, L. M. (2014). Spatial variation in the plasma sheet composition: Dependence on geomagnetic and solar activity. *Journal of Geophysical Research: Space Physics*, *119*, 2836–2857. <https://doi.org/10.1002/2013JA019517>
- Mauk, B. H., Fox, N. J., Kanekal, S. G., Kessel, R. L., Sibeck, D. G., & Ukhorskiy, A. (2013). Science objectives and rationale for the radiation belt storm probes mission. *Space Science Reviews*, *179*(1), 3–27. Retrieved from <https://doi.org/10.1007/s11214-012-9908-y>
- Mauk, B. H., & McIlwain, C. E. (1974). Correlation of Kp with the substorm-injected plasma boundary. *Journal of Geophysical Research*, *79*(22), 3193–3196. Retrieved from <https://doi.org/10.1029/JA079i022p03193>
- McIlwain, C. E. (1974). Substorm injection boundaries, *Magnetospheric physics: Proceedings of the advanced summer institute held at Sheffield, U.K., August 1973* (pp. 143–154). Dordrecht: Springer Netherlands.
- McPherron, R. L. (1970). Growth phase of magnetospheric substorms. *Journal of Geophysical Research*, *75*(28), 5592–5599. Retrieved from <https://doi.org/10.1029/JA075i028p05592>
- McPherron, R. L. (1972). Substorm related changes in the geomagnetic tail: The growth phase. *Planetary and Space Science*, *20*(9), 1521–1539. Retrieved from [https://doi.org/10.1016/0032-0633\(72\)90054-2](https://doi.org/10.1016/0032-0633(72)90054-2)
- McPherron, R. L., Russell, C. T., & Aubry, M. P. (1973). Satellite studies of magnetospheric substorms on August 15, 1968: 9. Phenomenological model for substorms. *Journal of Geophysical Research*, *78*(16), 3131–3149. Retrieved from <https://doi.org/10.1029/JA078i016p03131>
- Milan, S. E. (2009). Both solar wind-magnetosphere coupling and ring current intensity control of the size of the auroral oval. *Geophysical Research Letters*, *36*, L18101. Retrieved from <https://doi.org/10.1029/2009GL039997>
- Milan, S. E., Boakes, P. D., & Hubert, B. (2008). Response of the expanding/contracting polar cap to weak and strong solar wind driving: Implications for substorm onset. *Journal of Geophysical Research*, *113*, A09215. Retrieved from <https://doi.org/10.1029/2008JA013340>
- Milan, S. E., Grocott, A., Forsyth, C., Imber, S. M., Boakes, P. D., & Hubert, B. (2009). A superposed epoch analysis of auroral evolution during substorm growth, onset and recovery: Open magnetic flux control of substorm intensity. *Annales Geophysicae*, *27*(2), 659–668. Retrieved from <https://doi.org/10.5194/angeo-27-659-2009>
- Milan, S. E., Hutchinson, J., Boakes, P. D., & Hubert, B. (2009). Influences on the radius of the auroral oval. *Annales Geophysicae*, *27*(7), 2913–2924. Retrieved from <https://doi.org/10.5194/angeo-27-2913-2009>
- Milan, S. E., Lester, M., Cowley, S. W. H., Oksavik, K., Brittner, M., Greenwald, R. A., et al. (2003). Variations in the polar cap area during two substorm cycles. *Annales Geophysicae*, *21*(5), 1121–1140. Retrieved from <https://doi.org/10.5194/angeo-21-1121-2003>
- Milan, S. E., Provan, G., & Hubert, B. (2007). Magnetic flux transport in the Dungey cycle: A survey of dayside and nightside reconnection rates. *Journal of Geophysical Research*, *112*, A01209. Retrieved from <https://doi.org/10.1029/2006JA011642>
- Murphy, K. R., Watt, C. E. J., Mann, I. R., Jonathan Rae, I., Sibeck, D. G., Boyd, A. J., et al. (2018). The global statistical response of the outer radiation belt during geomagnetic storms. *Geophysical Research Letters*, *45*, 3783–3792. Retrieved from <https://doi.org/10.1002/2017GL076674>
- Nakai, H., & Kamide, Y. (2003). Substorm-associated large-scale magnetic field changes in the magnetotail: A prerequisite for “magnetotail deflation” events. *Annales Geophysicae*, *21*(4), 869–879. Retrieved from <https://doi.org/10.5194/angeo-21-869-2003>
- Nakamura, R., Nagai, T., Birn, J., Sergeev, V. A., Le Contel, O., Varsani, A., et al. (2017). Near-Earth plasma sheet boundary dynamics during substorm dipolarization. *Earth, Planets and Space*, *69*(1), 129. Retrieved from <https://doi.org/10.1186/s40623-017-0707-2>
- Newell, P. T., & Gjerloev, J. W. (2011). Evaluation of supermag auroral electrojet indices as indicators of substorms and auroral power. *Journal of Geophysical Research*, *116*, A12211. Retrieved from <https://doi.org/10.1029/2011JA016779>
- Ozeke, L. G., & Mann, I. R. (2001). Modeling the properties of high-m Alfvén waves driven by the drift-bounce resonance mechanism. *Journal of Geophysical Research*, *106*(A8), 15,583–15,597. Retrieved from <https://doi.org/10.1029/2000JA000393>
- Quinn, J. M., & Southwood, D. J. (1982). Observations of parallel ion energization in the equatorial region. *Journal of Geophysical Research*, *87*(A12), 10,536–10,540. Retrieved from <https://doi.org/10.1029/JA087iA12p10536>
- Reeves, G. D., Belian, R. D., & Fritz, T. A. (1991). Numerical tracing of energetic particle drifts in a model magnetosphere. *Journal of Geophysical Research*, *96*(A8), 13,997–14,008. Retrieved from <https://doi.org/10.1029/91JA01161>
- Reeves, G. D., Fritz, T. A., Cayton, T. E., & Belian, R. D. (1990). Multi-satellite measurements of the substorm injection region. *Geophysical Research Letters*, *17*(11), 2015–2018. Retrieved from <https://doi.org/10.1029/GL017i011p02015>
- Reeves, G. D., & Henderson, M. G. (2001). The storm-substorm relationship: Ion injections in geosynchronous measurements and composite energetic neutral atom images. *Journal of Geophysical Research*, *106*, 5833–5844. <https://doi.org/10.1029/2000JA003017>
- Reeves, G. D., Kettmann, G., Fritz, T. A., & Belian, R. D. (1992). Further investigation of the CDAW 7 substorm using geosynchronous particle data: Multiple injections and their implications. *Journal of Geophysical Research*, *97*(A5), 6417–6428. Retrieved from <https://doi.org/10.1029/91JA03103>
- Sandhu, J. K., Rae, I. J., Freeman, M. P., Forsyth, C., Gkioulidou, M., Reeves, G. D., et al. (2018). Energization of the ring current by substorms. *Journal of Geophysical Research: Space Physics*, *123*, 8131–8148. Retrieved from <https://doi.org/10.1029/2018JA025766>
- Sandhu, J. K., Yeoman, T. K., Fear, R. C., & Dandouras, I. (2016). A statistical study of magnetospheric ion composition along the geomagnetic field using the cluster spacecraft for l values between 5.9 and 9.5. *Journal of Geophysical Research: Space Physics*, *121*, 2194–2208. Retrieved from <https://doi.org/10.1002/2015JA022261>
- Sandhu, J. K., Yeoman, T. K., Rae, I. J., Fear, R. C., & Dandouras, I. (2017). The dependence of magnetospheric plasma mass loading on geomagnetic activity using cluster. *Journal of Geophysical Research: Space Physics*, *122*, 9371–9395. Retrieved from <https://doi.org/10.1002/2017JA024171>
- Sarris, E. T., Krimigis, S. M., & Armstrong, T. P. (1976). Observations of magnetospheric bursts of high-energy protons and electrons at 35 RE with IMP 7. *Journal of Geophysical Research*, *81*(13), 2341–2355. Retrieved from <https://doi.org/10.1029/JA081i013p02341>

- Sckopke, N. (1966). A general relation between the energy of trapped particles and the disturbance field near the Earth. *Journal of Geophysical Research*, *71*(13), 3125–3130. Retrieved from <https://doi.org/10.1029/JZ071i013p03125>
- Sergeev, V. A., Angelopoulos, V., & Nakamura, R. (2012). Recent advances in understanding substorm dynamics. *Geophysical Research Letters*, *39*, L05101. Retrieved from <https://doi.org/10.1029/2012GL050859>
- Spence, H. E., Reeves, G. D., Baker, D. N., Blake, J. B., Bolton, M., Bourdarie, S., et al. (2013). Science goals and overview of the Radiation Belt Storm Probes (RBSP) energetic particle, composition, and thermal plasma (ECT) suite on NASA's Van Allen Probes mission. *Space Science Reviews*, *179*(1), 311–336. Retrieved from <https://doi.org/10.1007/s11214-013-0007-5>
- Takada, T., Nakamura, R., Baumjohann, W., Asano, Y., Volwerk, M., Zhang, T. L., et al. (2006). Do BBFS contribute to inner magnetosphere dipolarizations: Concurrent cluster and double star observations. *Geophysical Research Letters*, *33*, L21109. Retrieved from <https://doi.org/10.1029/2006GL027440>
- Tanskanen, E. I. (2009). A comprehensive high-throughput analysis of substorms observed by image magnetometer network: Years 19932003 examined. *Journal of Geophysical Research*, *114*, A05204. Retrieved from <https://doi.org/10.1029/2008JA013682>
- Turner, N. E., Baker, D. N., Pulkkinen, T. I., & McPherron, R. L. (2000). Evaluation of the tail current contribution to Dst. *Journal of Geophysical Research*, *105*, 5431–5439. Retrieved from <https://doi.org/10.1029/1999JA000248>
- Turner, D. L., Fennell, J. F., Blake, J. B., Claudepierre, S. G., Clemmons, J. H., Jaynes, A. N., et al. (2017). Multipoint observations of energetic particle injections and substorm activity during a conjunction between magnetospheric multiscale (MMS) and Van Allen Probes. *Journal of Geophysical Research: Space Physics*, *122*, 11,481–11,504. Retrieved from <https://doi.org/10.1002/2017JA024554>
- Turner, D. L., O'Brien, T. P., Fennell, J. F., Claudepierre, S. G., Blake, J. B., Kilpua, E. K. J., & Hietala, H. (2015). The effects of geomagnetic storms on electrons in Earth's radiation belts. *Geophysical Research Letters*, *42*, 9176–9184. Retrieved from <https://doi.org/10.1002/2015GL064747>
- Wang, C.-P., Lyons, L. R., Weygand, J. M., Nagai, T., & McEntire, R. W. (2006). Equatorial distributions of the plasma sheet ions, their electric and magnetic drifts, and magnetic fields under different interplanetary magnetic field  $B_z$  conditions. *Journal of Geophysical Research*, *111*, A04215. Retrieved from <https://doi.org/10.1029/2005JA011545>
- Winglee, R. M. (2000). Mapping of ionospheric outflows into the magnetosphere for varying IMF conditions. *Journal of Atmospheric and Solar-Terrestrial Physics*, *62*, 527–540. [https://doi.org/10.1016/S1364-6826\(00\)00015-8](https://doi.org/10.1016/S1364-6826(00)00015-8)
- Yau, A. W., & Andre, M. (1997). Sources of ion outflow in the high latitude ionosphere. *Space Science Reviews*, *80*, 1–25. <https://doi.org/10.1023/A:1004947203046>
- Yue, C., Bortnik, J., Li, W., Ma, Q., Gkioulidou, M., Reeves, G. D., et al. (2018). The composition of plasma inside geostationary orbit based on Van Allen Probes observations. *Journal of Geophysical Research: Space Physics*, *123*, 6478–6493. Retrieved from <https://doi.org/10.1029/2018JA025344>
- Zaharia, S., Cheng, C. Z., & Johnson, J. R. (2000). Particle transport and energization associated with substorms. *Journal of Geophysical Research*, *105*(A8), 18,741–18,752. Retrieved from <https://doi.org/10.1029/1999JA000407>